Electronic Supplementary Information

Site-specific dynamic nuclear polarization in a Gd(III)-labeled protein

Jörg Heiliger,[abc] Tobias Matzel,[cd] Erhan Can Çetiner,[cd] Harald Schwalbe,*[cd] Georg Kuenze,*[ef] Björn Corzilius*[abcgh]

Phys. Chem. Chem. Phys., **2020**, DOI: 10.1039/d0cp05021k

[a] *Institute of Physical and Theoretical Chemistry, Goethe University Frankfurt, Max-von-Laue-Str. 7, 60438 Frankfurt am Main, Germany*

[b] *Institute of Biophysical Chemistry, Goethe University Frankfurt, Max-von-Laue-Str. 9, 60438 Frankfurt am Main, Germany*

[c] *Center for Biomolecular Magnetic Resonance (BMRZ), Goethe University Frankfurt, Max-von-Laue-Str. 9, 60438 Frankfurt am Main, Germany*

[d] *Institute of Organic Chemistry and Chemical Biology, Goethe University Frankfurt, Max-von-Laue-Str. 7, 60438 Frankfurt am Main, Germany. E-mail: schwalbe@nmr.uni-frankfurt.de*

[e] *Center for Structural Biology and Department of Chemistry, Vanderbilt University, 465 21st Ave S, Nashville, TN 37240, USA*

[f] *Institute for Drug Discovery, Leipzig University, Brüderstr. 34, 04103 Leipzig, Germany. E-mail: georg.kuenze@gmail.com*

[g] *Institute of Chemistry, University of Rostock, Albert-Einstein-Str. 3a, 18059 Rostock, Germany*

[h] *Department LL&M, University of Rostock, Albert-Einstein-Str. 25, 18059 Rostock, Germany. E-mail: bjoern.corzilius@uni-rostock.de*

Theory

General solid effect mechanism and its dependence on HFI

As the SE stringently relies on dipolar hyperfine interaction (HFI), the direct DNP transfer step is strongly dependent on the interconnecting vector between the electron and nuclear spin. Based on a minimal two-spin Hamiltonian in the frame rotating with the microwave (μw) frequency $\omega_{\mu w}$ around the external magnetic field direction, we must include the electron and nuclear Zeeman interaction as well as the secular and pseudo-secular part of the dipolar HFI:

$$\hat{H}_{\mathrm{SE}} = \left(\omega_{0S} - \omega_{\mu w}\right)\hat{S}_z - \omega_{0I}\hat{I}_z + A\hat{S}_z\hat{I}_z + B\hat{S}_z\hat{I}_x . \tag{S1}$$

Here, $\hat{S}_z$ and $\hat{I}_z$ are the projections of the electron and nuclear spin operator vectors, respectively, on the laboratory *z* axis (*i.e.*, the external magnetic field direction) in the two-spin product operator basis. $\omega_{0S} = \frac{g\mu_{\mathrm{B}}}{\hbar} B_0$ and $\omega_{0I} = \frac{g_{\mathrm{n}}\mu_{\mathrm{n}}}{\hbar} B_0$ are the electron and nuclear Zeeman frequencies, respectively, where g and g_{n} are the electron and nuclear g factors, μ_{B} and μ_{n} are the Bohr and nuclear magneton, respectively, $\hbar$ is the reduced Planck constant, and B_0 is the magnitude of external magnetic field. Finally, A is the secular and B the pseudo-secular HFI constant, given in the point-dipole approximation:

$$\begin{aligned} A &= d_{\mathrm{HFI}}\left(3\cos^2\theta - 1\right) \\ B &= 3d_{\mathrm{HFI}}\cos\theta\sin\theta \end{aligned} . \tag{S2}$$

θ is the angle between the external magnetic field and the e–n connecting vector. The typical inverse-cubic distance dependence is included in the dipole–dipole coupling constant (in the limit of isotropic Zeeman interaction):

$$d_{\mathrm{HFI}} = \frac{\mu_0}{4\pi}\frac{g\mu_{\mathrm{B}} g_{\mathrm{n}}\mu_{\mathrm{n}}}{\hbar} r^{-3}; \tag{S3}$$

with r being the e–n distance and μ_0 being the vacuum permeability.

The SE transition moment

By µw irradiation of the e–n spin pair with an oscillating field of amplitude B_{1S} and orientation perpendicular to B_0, an additional term is generated in the spin Hamiltonian. With the proper choice of reference frames,[S1] the effective µw Hamiltonian directly yields the transition moments between allowed EPR and "forbidden" e–n DQ and ZQ transitions:

$$\hat{H}'_{\mu w} = \omega_{1S}\hat{S}_x + \omega_{1S}\frac{B}{2\omega_{0I}}\hat{S}_x\hat{I}_x . \tag{S4}$$

Note that Eq. (S3) approximately applies in the high-field limit where $A, B \ll \omega_{0I}$.

During µw irradiation of one of the SE conditions with the Rabi frequency, $\omega_{1S} = \frac{g\mu_B}{\hbar}B_{1S}$, at the sum or difference of the electron and nuclear Larmor frequencies (*i.e.*, at $\omega_{\mu w} = \omega_{0S} \pm \omega_{0I}$), e–n DQ or ZQ coherences are generated by an effective field acting on these forbidden transitions with the DNP nutation frequency:

$$\omega_{DNP} = \frac{\omega_{1S}B}{2\omega_{0I}} = \frac{3\mu_0}{8\pi}\frac{g^2\mu_B^2}{\hbar}\frac{B_{1S}}{B_0}r^{-3}\cos\theta\sin\theta . \tag{S5}$$

DNP transfer dynamics

Next, we describe the polarization dynamics within the e–n pair which may be expressed by a general rate equation:

$$\frac{d}{dt}\mathbf{p} = \left(\mathbf{W} + \mathbf{R}_1\right)\mathbf{p} . \tag{S6}$$

With this equation the state of the whole spin system is described by the population vector **p** which spans over the individual populations $p_i = \rho_{ii}$ of all spin states *i*. **W** is a rate matrix which contains all possible µw-induced transitions (*i.e.*, EPR and DNP) while $\mathbf{R}_1$ is a relaxation matrix driving the population vector back to its thermal equilibrium state. The use of Eq. (S6) is valid, as long as the build-up of coherences between eigenstates can be neglected (*i.e.*, the decoherence rate is much

larger than any µw-driven transition rate). This condition is reasonably met in the case of SE DNP under MAS.

For didactical reasons we simplify the master equation to the specific case of direct µw excitation of one SE DNP transition where only two electron spin states are involved, namely $\left|m_S=-\tfrac{1}{2},m_I=+\tfrac{1}{2}\right\rangle \rightarrow \left|m_S=+\tfrac{1}{2},m_I=-\tfrac{1}{2}\right\rangle$. This is the ZQ transition for a nucleus with positive g_n and results in positive DNP enhancement (for a nucleus with negative g_n the signs of m_I have formally to be inverted for the DQ transition which also results in positive DNP). For this isolated transition, a simple rate equation can be derived:

$$\frac{\mathrm{d}}{\mathrm{d}t}\begin{pmatrix}P_\mathrm{e}\\P_\mathrm{n}\end{pmatrix}=\begin{pmatrix}-k_\mathrm{DNP}-R_\mathrm{1e} & +k_\mathrm{DNP}\\ +k_\mathrm{DNP} & -k_\mathrm{DNP}-R_\mathrm{1n}\end{pmatrix}\begin{pmatrix}P_\mathrm{e}\\P_\mathrm{n}\end{pmatrix}+\begin{pmatrix}P_\mathrm{e}^\circ R_\mathrm{1e}\\P_\mathrm{n}^\circ R_\mathrm{1n}\end{pmatrix}. \tag{S7}$$

In the limit where electron relaxation is sufficiently fast in order to always maintain $P_\mathrm{e}=P_\mathrm{e}^\circ$, we get:

$$\frac{\mathrm{d}}{\mathrm{d}t}\frac{P_\mathrm{n}}{P_\mathrm{n}^\circ}=k_\mathrm{DNP}\left(\varepsilon_\mathrm{max}-\frac{P_\mathrm{n}}{P_\mathrm{n}^\circ}\right)+R_\mathrm{1n}\left(1-\frac{P_\mathrm{n}}{P_\mathrm{n}^\circ}\right). \tag{S8}$$

From this rate equation we can derive two measures: (i) the steady-state enhancement factor, as well as (ii) the initial DNP rate.

Steady-state DNP enhancement factor

This enhancement factor ε_∞ is obtained once the system has reached a dynamic equilibrium at sufficiently long (ideally infinite) polarization time. Therefore, it may be expressed as a function of an equilibrium constant K_DNP:[S2]

$$\varepsilon_\infty=\frac{1+K_\mathrm{DNP}\varepsilon_\mathrm{max}}{1+K_\mathrm{DNP}} \tag{S9}$$

which is defined by the ratio between the DNP build-up rate constant k_DNP and the longitudinal relaxation rate constant R_1n:

$$K_{\mathrm{DNP}} = \frac{k_{\mathrm{DNP}}}{R_{1\mathrm{n}}}. \tag{S10}$$

Since $R_{1\mathrm{n}}$ is depending on the e–n distance in a non-trivial manner, K_{DNP} is as well expected to depend on r. In order to analyze this dependence, we first derive k_{DNP} which is proportional to the respective SE transition probability following Fermi's Golden Rule and thus scales as the square of the transition moment given in Eq. (S5). Therefore, k_{DNP} is expected to follow a r^{-6} law for a direct e–n transfer:

$$k_{\mathrm{DNP}} = \left(\frac{3\mu_0}{8\pi} \frac{g^2 \mu_{\mathrm{B}}^2}{\hbar} \frac{B_1^{(\mu\mathrm{w})}}{B_0} \right)^2 r^{-6} \cos^2\theta \sin^2\theta \left[S(S+1) + \frac{1}{4} \right] \cdot G(\omega_{\mu\mathrm{w}}). \tag{S11}$$

This description is valid for any electron spin with half-integer quantum number S, but is limited on the central transition as is described above. Therefore, the penultimate term is derived from the Clebsch-Gordan coefficients following the scaling factor $\sqrt{S(S+1) - m_S(m_S - 1)}$ with $m_S = \frac{1}{2}$.[S3] Finally, the last term reflects the line shape function and is in the simplest case represented by a Lorentzian.

The dipolar paramagnetic relaxation enhancement (PRE) can be in the most general case described by [S4]:

$$R_{1\mathrm{n}}^{(\mathrm{dip})} = \frac{2}{15} \left(\frac{\mu_0}{4\pi} \right)^2 \frac{g^2 g_{\mathrm{n}}^2 \mu_{\mathrm{B}}^2 \mu_{\mathrm{n}}^2}{\hbar^2} r^{-6} S(S+1) \cdot f(\tau_{\mathrm{c}}). \tag{S12}$$

Here, $f(\tau_{\mathrm{c}})$ describes the spectral density functions at the nuclear Larmor frequency as well as at the e–n ZQ and DQ frequencies as is described by Solomon's theory.[S5] As both PRE and DNP depend on the squared HFI coupling, they follow the same theoretical distance law. Therefore, as long as dipolar PRE is the only nuclear relaxation mechanism, the steady-state DNP enhancement is in theory independent of the interspin distance within the e–n pair, which can be seen by inserting Eqs. (S11) and (S12) into (S10):

$$K_{\mathrm{DNP}}^{\circ} = \frac{k_{\mathrm{DNP}}}{R_{1\mathrm{n}}^{(\mathrm{dip})}} = \frac{135}{8} \left(\frac{\omega_{1S}}{\omega_{0I}} \right)^2 \cos^2\theta \sin^2\theta \left[1 + \frac{1}{4S(S+1)} \right] \frac{G(\omega_{\mu\mathrm{w}})}{f(\tau_{\mathrm{c}})}. \tag{S13}$$

However, this situation is different if paramagnetic dipolar relaxation is not the dominant mechanism and other spin-lattice relaxation sources are present. Then, an additional relaxation rate has to be accounted for:

$$R_{1n} = R_{1n}^{(dip)} + R_{1n}^{\circ}\,, \tag{S14}$$

which breaks the exact cancellation of the e–n distance dependence within the equilibrium constant:

$$K_{DNP} = \frac{k_{DNP}}{R_{1n}^{(dip)} + R_{1n}^{\circ}}\,. \tag{S15}$$

As a result, a distance-dependent DNP enhancement factor ε_∞ is now expected because the additional spin-lattice relaxation rate constant R_{1n}° may feature an arbitrary or no dependence with respect to *r*. Due to this rather unpredictable behavior, the enhancement factor is not a reliable measure for e–n distance.

Initial DNP build-up rate

The initial DNP rate may be directly obtained by analyzing the build-up of nuclear polarization immediately after initiating the DNP transfer, for example by turning on the µw field:

$$k_{DNP}^{\circ} = \frac{\mathrm{d}}{\mathrm{d}t}\frac{P_n}{P_n^{\circ}}\bigg|_{t=0} = k_{DNP}\left(\varepsilon_{max} - 1\right). \tag{S16}$$

This initial DNP rate k_{DNP}° is directly proportional to r^{-6}, however, it is rather inconvenient to measure in an MAS DNP setup because a full equilibration of magnetization has to be allowed in the absence of µw before the µw field is turned on for each transient/time point of the build-up curve which is exceptionally time-consuming (considering T_{1n} being on the order of 100 to 1000 s for low-γ nuclei at 100 K); additionally it is inconvenient or even impossible with most gyrotron sources which cannot easily be gated.

Alternatively, the nuclear polarization can be depleted by an rf pulse train before allowing enhanced polarization to be built up by DNP. In this case, experiments are only delayed by the

short saturation train of ~100 ms and a short recycle period in order to reduce the pulse duty cycle. Unfortunately, the system starts in this case from a state off thermal equilibrium and the initial DNP rate is now also a function of R_{1n}:

$$k_{DNP}^{\circ} = \frac{d}{dt}\frac{P_n}{P_n^{\circ}}\bigg|_{t=0} = k_{DNP}\varepsilon_{max} + R_{1n} . \tag{S17}$$

By separating R_{1n} into its separate contributions following Eq. (S14), we can define a term which depends on r^{-6}, and another term which has a different distance dependence:

$$k_{DNP}^{\circ} = \frac{d}{dt}\frac{P_n}{P_n^{\circ}}\bigg|_{t=0} = \underbrace{k_{DNP}\varepsilon_{max} + R_{1n}^{(dip)}}_{=f\left(r^{-6}\right)} + \underbrace{R_{1n}^{\circ}}_{\neq f\left(r^{-6}\right)} \tag{S18}$$

The contribution from the "background" spin-lattice relaxation rate R_{1n}° may look unsettling at first glance since it seems to prevent a clear r^{-6} dependence which is sought-after for quantitative analysis of e–n distances by DNP. However, by utilizing Eq. (S9), we see that in order to achieve sizeable DNP enhancement factors (*i.e.*, $\varepsilon_{\infty} \gg 1$) it must always be the case that $k_{DNP}\varepsilon_{max} \gg R_{1n} \geq R_{1n}^{\circ}$. Thus, Eqs. (S17) and (S16) are approximately equal at large enhancement factors.

Materials and Methods

Protein expression and labeling

The G75C mutant of human ubiquitin described in Kaushik *et al*.[1] was recombinantly expressed from *E. coli* strain BL21(DE3) in M9 minimal medium (2 g ^{13}C-glucose and 1 g $^{15}NH_4Cl$ per liter), LB medium (Carl Roth GmbH & Co. KG, Karlsruhe, Germany) or OD2 CDN medium (Silantes GmbH, Munich, Germany). The respective media used for the different isotope labelling schemes can be taken from Table S1. The cells grown in deuterated M9 media were stepwise (30 %, 60 %, 90 %) adapted to the higher D_2O concentrations in 50 mL precultures.

Table S1. Media used for the respective achieved isotope labelling.

Isotope labelling scheme	Medium used
No isotope labelling	LB-medium
^{13}C, ^{15}N	M9
^{13}C, ^{15}N, ^{2}H (30 %)	M9 30 % D_2O
^{13}C, ^{15}N, ^{2}H (60 %)	M9 60 % D_2O
^{13}C, ^{15}N, ^{2}H (90 %)	M9 90 % D_2O
^{13}C, ^{15}N, ^{2}H (100 %)	OD2 CDN medium

All samples were purified as follows. The harvested cells were resuspended in 50 mM NH_4OAc (pH = 7.0) with 10 mM β-mercaptoethanol, lysed and centrifuged at 16000 rpm for 45 minutes. The pH of the lysate was adjusted to 5.0 with 10% AcOH and subsequently heated to 85 °C for 15 minutes. The precipitate was removed by centrifugation (8,000 g for 30 min) and decantation. The

supernatant was sterile filtered and further purified over a HisTrap SP HP 5 mL cation exchange column using a 50 mM to 500 mM NH_4OAc (pH = 5.0) concentration gradient.

The fractions containing ubiquitin were identified by SDS-PAGE, pooled together and the NH_4OAc buffer was exchanged to H_2O. Subsequently 200 µM of the protein were incubated with 30 mM DTT at 37 °C for 2 h to remove disulfide bridges formed with β-mercaptoethanol during purification. Impurities were removed using a PD-10 desalting column. The protein solution was mixed with 1 M NH_4OAc in ratio 3:1 and incubated with MMA-DOTA in a twofold excess over night at 37 °C. The unreacted spin label was removed during buffer exchange to H_2O and the Gd^{3+} ion was added. The sample was lyophilized and transferred to D_2O, to deuterate all exchanging protons. The spin labeling efficiency was determined by EPR.

Mass spectrometry

The degree of deuteration was determined by MALDI mass spectroscopy. The expected m/z values were calculated for each mutant assuming different isotope labeling schemes with full isotope substitution (see Table S2). The experimental values were determined for different mutants and protein deuteration ratios after triple lyophilization from (i) D_2O as well as (ii) H_2O. This ensures that all exchangeable hydrogens are either ^1H or ^2H. Respective solvents (H_2O/ D_2O) were also used for the solubilization of the matrix. The samples were measured on a Voyager-DE™ STR Biospectrometry Workstation. From the experimental *m*/*z* values, the deuteration ratio has been calculated by the following formula (see Table S3):

$$\text{deuteration ratio} = \frac{\text{experimental} - \text{calculated}(0\ \%)}{\text{calculated}(100\ \%) - \text{calculated}(0\ \%)}. \qquad \text{(S19)}$$

Table S2. Calculated mass numbers for fully isotope labeling of ubiquitin. Values are given as *m*/*z* ratio for singly charged proteins.

mutant	$^{1}H,^{12}C,^{14}N$	$^{1}H,^{13}C,^{15}N$	$^{2}H,^{13}C,^{15}N$
F4C	8,521	8,998	9,623
A28C	8,597	9,080	9,709
G75C	8,611	9,095	9,726

Table S3. Experimental *m*/*z* values for isotope labeled samples.

sample	calculated		experimental		ratio	
	0%	100%	D_2O	H_2O	D_2O	H_2O
[DCN]-F4C-Ub	8,998	9,623	9,538	9460	86%	74%
[DCN]-A28C-Ub	9,080	9,709	9,637	9,537	89%	73%
[DCN]-G75C-Ub	9,095	9,726	9,641	9,565	87%	74%
[0.9DCN]-G75C-Ub	9,095	9,726	9,516	9,461	67%	58%
[0.6DCN]-G75C-Ub	9,095	9,726	9,440	9,377	55%	45%
[0.3DCN]-G75C-Ub	9,095	9,726	9,292	9,226	31%	21%
[CN]-G75C-Ub	9,095	9,726	9,156	9,092	10%	0%

$^{1}H,^{15}N$-HSQC based PRE-Experiment

The PRE-NMR experiments were acquired on samples with protein concentrations of 600 µM in a buffer containing 30 mM sodium acetate (pH 4.7) and 50 mM sodium chloride. The samples

contained 10% (v/v) D_2O and 100 µM trimethylsilylpropanoic acid (TSP) as internal reference. Nitrogen shifts were indirectly referenced using the chemical shift ratio $\delta(^{15}N) = 0.101329118\ \delta(^{1}H)$.[S6] Measurements were carried out at room temperature in 5 mm NMR-tubes at a Bruker Avance III HD (600 MHz) spectrometer equipped with a triple resonance cryoprobe. All spectra were processed with Topspin (Bruker) and analyzed with Sparky[S7] using the assignment published by Wang *et al.*[S8] The ^{1}H, ^{15}N-HSQC-based pulse sequence according to Iwahara *et al.*[S9] was used and the experimental PRE-rates were determined using the single-time-point approach with a delay of 8 ms.[S10, 11] As diamagnetic reference to the Gd-DOTA-labeled protein Lu-DOTA-M-labeled ubiquitin (^{1}H, ^{15}N) was used.

DNP-enhanced MAS NMR

Preparation of DNP samples

For SCREAM-DNP experiments four samples of L-methionine-(methyl-^{13}C,D_3), L-methionine-(methyl-^{13}C,D_2), L-methionine-(methyl-^{13}C,D_1), and L-methionine-(methyl-^{13}C) were dissolved at a concentration of 100 mM in a D_8-$^{12}C_3$-glycerol/D_2O/H_2O (60/30/10 vol.-%) mixture together with 10 mM AMUPol (SATT Sud-Est, Marseille). D_2O (99.9% D) was purchased from Sigma-Aldrich (Merck); deuterated and ^{13}C-depleted (98% D, 99.95% ^{12}C) glycerol was purchased from Eurisotop (CIL). 30 µL of each final solution was transferred into a 3.2 mm sapphire MAS sample rotor (Bruker) closed with a vespel drive tip (Bruker). A silicone soft plug (Bruker) was used for sealing.

For field calibration experiments 2 M ^{13}C-$^{15}N_2$-Urea (99% ^{13}C, 98% ^{15}N, CortecNet) was dissolved in a D_8-$^{12}C_3$-glycerol/D_2O/H_2O (60/30/10 vol.-%) mixture together with 5 mM Gd-DOTA (gracious gift of J. Plackmeyer, Frankfurt). 30 µL of the final solution was transferred into a 3.2 mm sapphire MAS sample rotor (Bruker) closed with a vespel drive tip (Bruker). A silicone soft plug (Bruker) was used for sealing.

For all protein-detecting experiments a mixture of D_8-$^{12}C_3$-glycerol (98% D, 99,95% ^{12}C, Eurisotop (CIL)) and D_2O (99.9% D, Sigma-Aldrich (Merck)) were added so that a final solution of ~1.0 mM protein (Table S4) in D_8-$^{12}C_3$-glycerol/D_2O (60/40 vol.-%) was obtained. 30 µL of each final solution was transferred into a 3.2 mm sapphire MAS sample rotor (Bruker) closed with a vespel drive tip (Bruker). A silicone soft plug (Bruker) was used for sealing.

Table S4. Protein concentrations of the DNP samples.

mutant	concentration (mM)
[CN]-G75C-Ub	1.17
[0.3DCN]-G75C-Ub	1.05
[0.6DCN]-G75C-Ub	1.18
[0.9DCN]-G75C-Ub	2.09
[DCN]-G75C-Ub	0.94
[DCN]-F4C-Ub	1.00
[DCN]-A28C-Ub	1.00

DNP experiments

The measurements of protein samples were performed on a Bruker Avance III spectrometer operating at 401.7 MHz ^1H frequency using a commercially available Bruker Ascend DNP magnet (89 mm), centered at 9.40 T and containing a superconducting sweep coil with a nominal range of ±75 mT. A Bruker gyrotron yielding 263.4 GHz microwaves, operating at the maximum beam current of 115 mA was used. The optimum field position was set with the help of a Gd-DOTA

reference sample (see above). Experiments were performed at ~120 K (µw on) or ~112 K (µw off), read out via a thermocouple inside the MAS stator.

Experiments on Methionine samples were carried out using a commercially available Bruker AVANCE II DNP spectrometer operating at 400.2 MHz ^{1}H frequency with a Bruker Ultrashield 9.4 T widebore (89 mm) magnet. A Bruker gyrotron with 60 mA of beam current produced 263.4 GHz microwaves. Experiments were performed at ~112 K (µw on) or ~104 K (µw off), read out via a thermocouple inside the MAS stator.

For all experiments radio frequency (rf) pulse powers were set to 100 kHz, 50 kHz, and 40 kHz for ^{1}H, ^{13}C, and ^{15}N. SPINAL64 at 100 kHz was used for broadband decoupling of ^{1}H magic-angle spinning (MAS) with spinning frequency of 8 kHz was used for all experiments. All direct polarization spectra were measured using a single 90° pulse excitation after a pre-saturation pulse train (consisting of 16 90° pulses separated by 3 ms each) applied to ^{13}C/^{15}N and subsequent variable polarization delay as given in the text. SPINAL64 was utilized during detection.

Were applicable, spectra were normalized by division through the number of accumulated transients and/or protein concentration.

Determination of initial DNP rates

Direct DNP-enhanced ^{15}N-MAS spectra were recorded at varying polarization times with different numbers of accumulations to optimize the experimental time for maximum SNR for the rather weak intensities at short polarization delays: 2048 scans at 1 and 2 s, 1024 scans at 4 s, 512 scans at 8, 10, and 16 s, 128 scans at 32 s, 64 scans at 64 and 128 s and 32 scans at 256 and 512 s. Spectra were then baseline corrected around the region encompassing each side chain resonance and integrated over the range shown in Figure S4A. To avoid negative signs due to operation at the negative SE DNP conditions, the sign of the integral was inverted.

From the acquired build-up curves the initial DNP rates were determined by linear fitting of the early data points between 1 and 16 s (between 1 and 10 s for A28C Arg) in Origin Pro 2020 and

the cumulative DNP rate was taken from the slope (see Figure S4B); the error bars were determined by the error calculated from the fit. In the case of A28C His and G75C His no reasonable fit could be achieved due to insufficient SNR and large scatter of the intensities both above and below zero. For F4C Arg, the intensities of the shortest polarization delays are highly scattered, and an overall linear behavior is observed without the typical plateau characteristic of an exponential build-up as can be seen in all other cases (except His of A28C and G75C as mentioned earlier). Therefore, we followed a bootstrapping approach where we included all data points for the fit (solid line in Figure S4B) and subsequently removed the last as well as the two last data points (*i.e.*, 256 and 512 s); the resulting fits diverged insignificantly considering the much larger absolute slope of the other mutants. The slope of the three fits where then averaged, and the error bars were determined from the overall span of the maximum and minimum slope including the respective errors. The averaged initial DNP rate $\left\langle k^{\circ}_{\mathrm{DNP}} \right\rangle$ was finally calculated by division of the cumulative rate (slope) by the overall number of the side chain nitrogens of each amino acid (*i.e.*, 12 for Arg, 7 for Lys, and 2 for His) and is given in Table 2.

Structural modeling of Gd-DOTA-M tags in ubiquitin

The structure of a Gd-DOTA-M tag conjugated to the side chain of cysteine (Gd-DOTA-M-Cys) was built with Avogadro (version 1.2),[S12] starting from the crystallographic structure of 10-(2-hydroxylpropyl)-1,4,7,10-tetra-azacyclododecane 1,4,7-tetraacetate.[S13] Because the reaction of Gd-DOTA-M with cysteine creates a new stereogenic center at the maleimide ring, the structure of Gd-DOTA-M-Cys was built in two absolute configurations (R and S). Structure geometry was optimized by DFT calculations with Gaussian09 (Gaussian, Inc., Wallingford CT) using the quasi-relativistic effective core potential (ECP)[S14] and [5s4p3d]-GTO valence basis sets for the Gd^{3+} ion, the 6-31(d,p) standard basis set for the ligand atoms, and the PBE1PBE functional.[S15] Solvation effects were evaluated with the integral equation formalism of the polarizable continuum model (IEFPCM)[S16] implemented in Gaussian09.

The BCL::ConformerGenerator method[S17] was used to build a library of 3000 unique conformations for both the S- and R-form of Gd-DOTA-M-Cys. The method generates 3D ligand conformers by combining rotamers of known small molecule structures from the Crystallography Open Database (COD)[S18, 19] according to a statistically-derived Boltzmann energy. In conformer generation, the linker connecting the backbone Cα-atom with the DOTA part of the spin label residue was fully flexible while the conformation of the Gd-DOTA moiety was treated as rigid. A total of 30,000 conformer generation iterations were carried out from which the 3000 best-scoring linker conformations were kept after removing similar conformers with a pairwise root-mean-squared distance deviation (RMSD) <0.25 Å. The conformer library was deemed nearly complete as all of the expected rotamers of the six linker dihedral angles (χ_1 to χ_6) occurred with similar probabilities (Figure S5).

The Rosetta software (version 3.12)[S20] was used to model the conformations of Gd-DOTA-M-Cys at each of the three experimentally studied spin label sites (F4, A28, G75) in ubiquitin (Figure S5). To this end, the native protein residue was successively replaced by every conformer of the S- and R-isomer of Gd-DOTA-M-Cys after aligning the corresponding backbone atoms of protein and spin label residue with each other. Rosetta atom types and partial charges for Gd-DOTA-M-Cys were assigned as described previously.[S21] The backbone and side chain degrees of freedom of all protein residues surrounding the Gd-DOTA-M-Cys spin label were minimized using the Rosetta all-atom ref2015 energy function[S22] while applying weak distance constraints between all pairs of Cα-atoms which were within 10 Å of each other. Spin label conformers which still clashed with the protein after minimization according to a Rosetta energy cutoff (> −100 kcal/mol) were removed. To account for protein conformational flexibility, we applied this procedure to an ensemble of ubiquitin structures, which was generated by relaxing each of the ten members of the NMR-determined structural ensemble of ubiquitin (PDB: 1D3Z)[S23] with Rosetta FastRelax[S24]. The FastRelax refinement protocol searches low-energy conformations around the starting structure by performing interlaced cycles of side chain repacking and minimization of all backbone and side chain torsion angles while ramping up and down the repulsive weight of the Rosetta energy function. In case of

spin label site G75, an additional 30 protein models, which were obtained by clustering a molecular dynamics trajectory of ubiquitin, were used for FastRelax refinement. This was done to increase the conformational sampling at G75, because this residue, which is located one position before the ubiquitin C-terminus, was assumed to be more flexible than residues F4 and A28.

Based on the modeled conformational ensembles of Gd-DOTA-M-Cys at each of the three spin label sites, distance distributions and effective distances between the Gd^{3+} ion and the side chains of Arg, Lys, and His residues in ubiquitin were calculated. To this end, the distance between the Gd^{3+} ion of each conformer in the spin label ensemble and the center of mass of the side chain nitrogen atoms of each Arg (Nε, $N\eta^1$, $N\eta^2$), Lys (Nξ), or His ($N\delta^1$, $N\varepsilon^2$) residue was measured. The effective distance was then calculated according to:

$$\bar{r} = \left(\frac{1}{n \cdot m} \sum_{i=1}^{n} \sum_{j=1}^{m} r_{\mathrm{Gd},i-\mathrm{aa},j}^{-6} \right)^{-\frac{1}{6}} \tag{S20}$$

where the first sum runs over all *n* valid conformers *i* of Gd-DOTA-M-Cys at a given spin label site, and the second sum runs over all *m* individual residues *j* that are either Arg (R42, R54, R72, R74), Lys (K6, K11, K27, K29, K33, K48, K63) or His (H68), respectively. Because we assumed that the protein existed as rigid, slow-exchanging ensemble under the cryogenic conditions of the DNP experiment, $\bar{r}$ was calculated for each structural model of ubiquitin separately, and the mean value of $\bar{r}$ over all ten (or 40 in case of G75C) models was used for further analysis.

For means of comparing the modeled conformational ensembles of Gd-DOTA-M-Cys with experimental $^1H^N$ PRE data, PRE rates were back-calculated from the model structures using the approach by Iwahara et al.[S25] Experimental PREs were estimated from the HSQC cross-peak intensity ratios of Gd^{3+} (paramagnetic) and Lu^{3+} (diamagnetic)-tagged ubiquitin (I_{Gd}/I_{Lu}) using the approach by Battiste and Wagner.[S10] PREs were capped at 60 Hz which for Gd^{3+}-tagged ubiquitin corresponds to a I_{Gd}/I_{Lu} value of ca. 20%. Below this cutoff, the Gd^{3+}-nuclear spin distance and I_{Gd}/I_{Lu} ratio are no longer linearly dependent and small deviations in signal intensity can result in

large PRE calibration errors. The agreement between experimental (exp) and calculated (calc) PREs was evaluated with the PRE Q-factor:[S25]

$$Q_{\mathrm{PRE}} = \sqrt{\frac{\sum_i \left(\Gamma_i^{(\mathrm{exp})} - \Gamma_i^{(\mathrm{calc})} \right)^2}{\sum_i \left(\Gamma_i^{(\mathrm{exp})} \right)^2}} \qquad \text{(S21)}$$

The following constants were used for the simulation of PREs: ^{1}H gyromagnetic ratio γ_{H} = $267.51 \cdot 10^6$ rad s^{-1} T^{-1}, Bohr magneton $\mu_{\mathrm{B}} = 9.274 \cdot 10^{-24}$ J T^{-1}, vacuum permeability $\mu_0 = 1.257 \cdot 10^{-6}$ N A^{-2}, spin quantum number for Gd^{3+} $S = 3.5$, electron g-factor $g = 2.0$, ^{1}H resonance frequency $\omega_{\mathrm{H}} = 3.77 \cdot 10^9$ rad s^{-1}. The effective correlation time τ_{c} was optimized by a grid search: 4.0 ns for F4C-Ub, 4.5 ns for A28C-Ub, and 2 ns for G75C-Ub.

Additional Figures

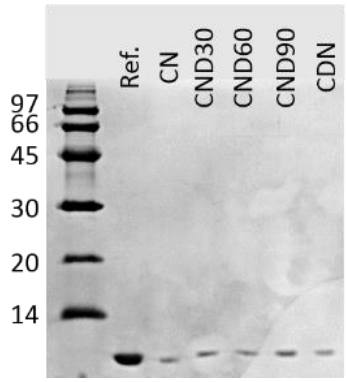

Figure S1. 12.5 % SDS-Gel of the different isotope labeled G75C-Ub constructs.

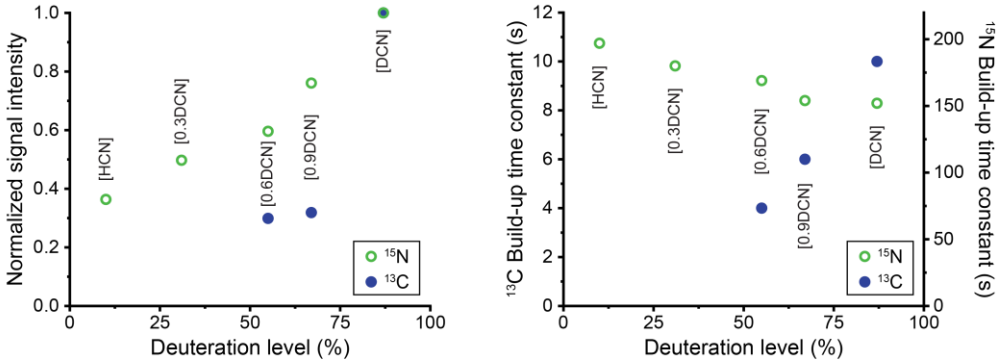

Figure S2. Normalized signal intensities (left) and DNP build-up time constants of Gd-G75-Ub at different protein deuteration levels.

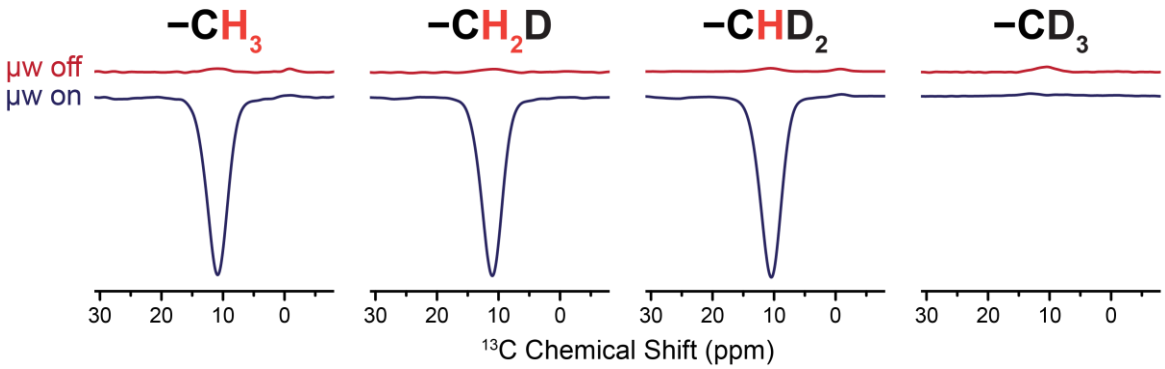

Figure S3. Comparison of cross-relaxation behaviour of (partially) deuterated methyl groups. Spectra shown are recorded by a direct polarization experiment (Bloch decay) with or without µw irradiation under typical DNP conditions with AMUPol as polarizing agent. Specific cross-relaxation enhancement by active motions under DNP (SCREAM-DNP) leads to an inversion of the ^{13}C methyl group of L-methionine through ^{1}H–^{13}C cross-relaxation as is described in detail by Aladin and Corzilius.[S26] This effect is of equal efficiency independent of deuteration level of the methyl group as long as at least one proton is included in the methyl group.

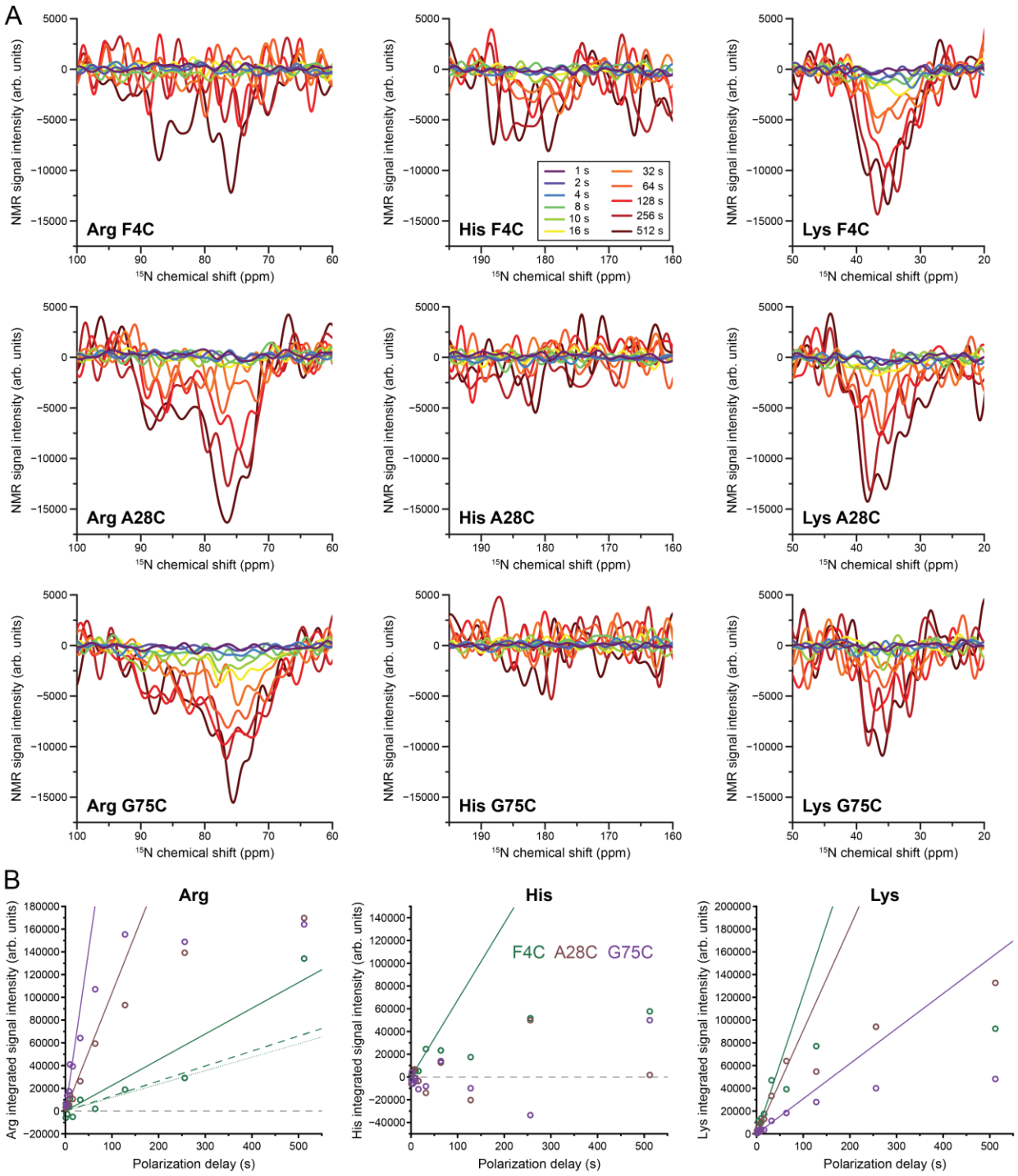

Figure S4. Determination of experimental initial DNP build-up rates. (A) Direct ^{15}N-enhanced NMR spectra of Arg, His, and Lys side chains for the three mutants recorded at different polarization times. (B) Signal intensities obtained by integrating the spectra in (A) over the shown range. Rates were determined by the slope of linear fits of the early data points as is described on page S13f.

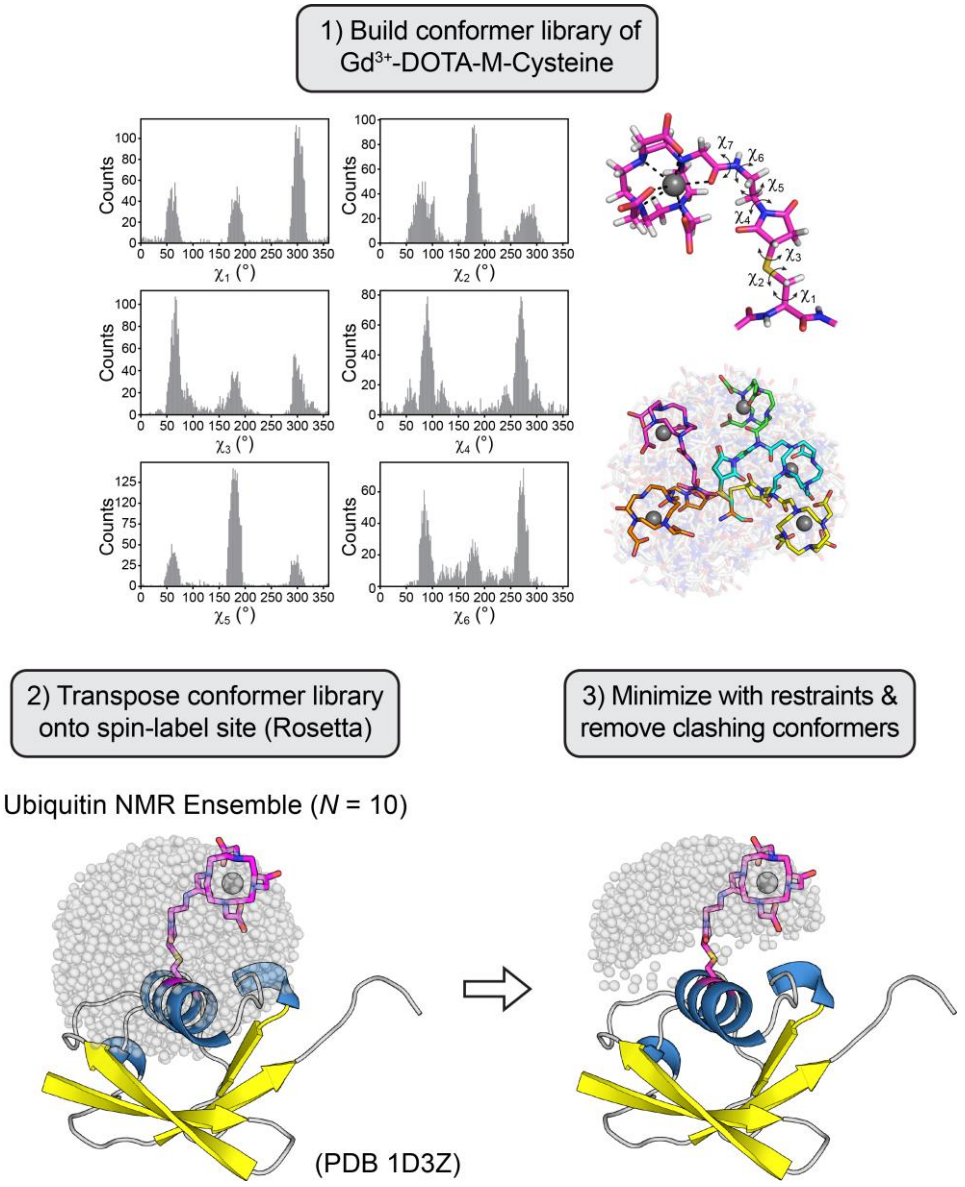

Figure S5. Overview of the computational protocol used for exhaustively simulating the conformations of Gd-DOTA-M-Cys spin labels when attached to ubiquitin. A conformer library of the flexible linker, which connects the protein backbone to the DOTA chelator, is generated by sampling from known small molecule structures in the Crystallography Open Database (COD) using the BCL::ConformerGenerator method.[S17] The Gd-DOTA-M-Cys conformer library is transposed to the protein spin label site by aligning the amino acid backbone atoms of each conformer with the corresponding protein backbone atoms for each member of the NMR structural ensemble of ubiquitin (PDB 1D3Z).[S23] For each Gd-DOTA-M-Cys conformer, the protein and spin label structures are minimized with Cα-atom pair distance restraints using the Rosetta software.[S20] The interaction energy of each conformer with the protein is then calculated using the Rosetta all-atom ref2015 energy function[S22] to identify clashing conformers which are subsequently removed.

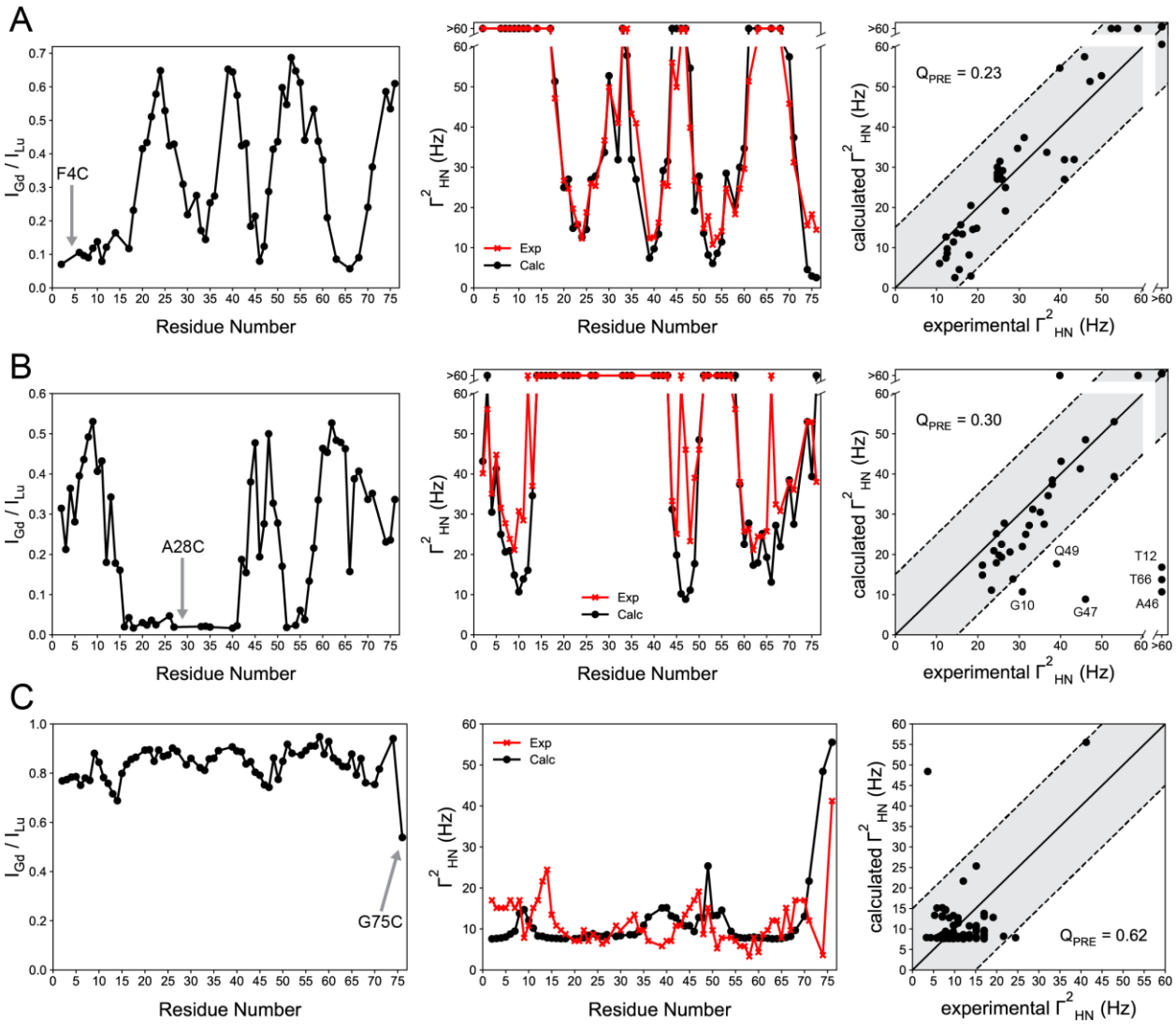

Figure S6. Comparison between experimental and model-predicted $^{1}H^{N}$ PREs of Gd-DOTA-M-tagged ubiquitin. (A) Gd-F4C-Ub. (B) Gd-A28C-Ub. (C) Gd-G75C-Ub. For each tagging position the following graphs are shown: Intensity ratio of $^{1}H/^{15}N$-HSQC cross-peaks of Gd-tagged ubiquitin relative to the diamagnetic control (Lu^{3+}) versus the primary sequence of ubiquitin (left), $^{1}H^{N}$ PREs derived from the analysis of experimental I_{Gd}/I_{Lu} values or back-calculated from structural models of Gd-tagged ubiquitin, respectively, versus the primary sequence of ubiquitin (middle), correlation between experimental and back-calculated PREs (right). PREs were capped at a cutoff of 60 Hz which corresponds to a I_{Gd}/I_{Lu} ratio of ca. 20%. Below this cutoff, small deviations in signal intensity can result in large PRE calibration errors. The Q-factor between experimental and back-calculated PREs (excluding pairs for which the experimental PRE was capped at 60 Hz) is indicated.

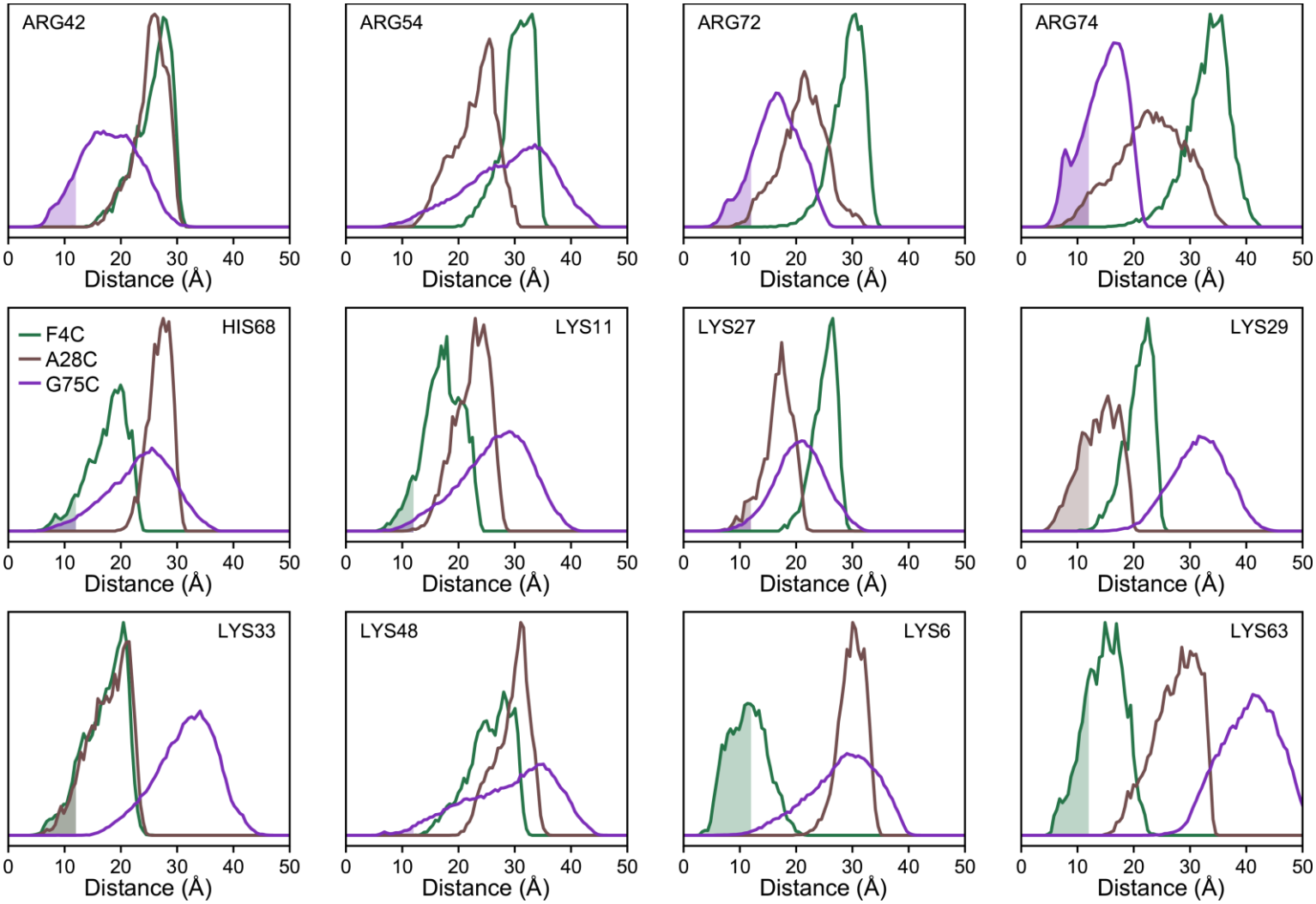

Figure S7. Distributions of Gd^{3+}–^{15}N distances calculated from models of Gd-F4C-Ub (green), Gd-A28C-Ub (brown), and Gd-G75-Ub (purple). Each plot shows the relative frequency of occurrence of the distance between the Gd^{3+} and the center of mass of each side-chain's ^{15}N system. The shaded area of the histograms marks distances that are equal or below 12 Å. For further details, see the description in the text.

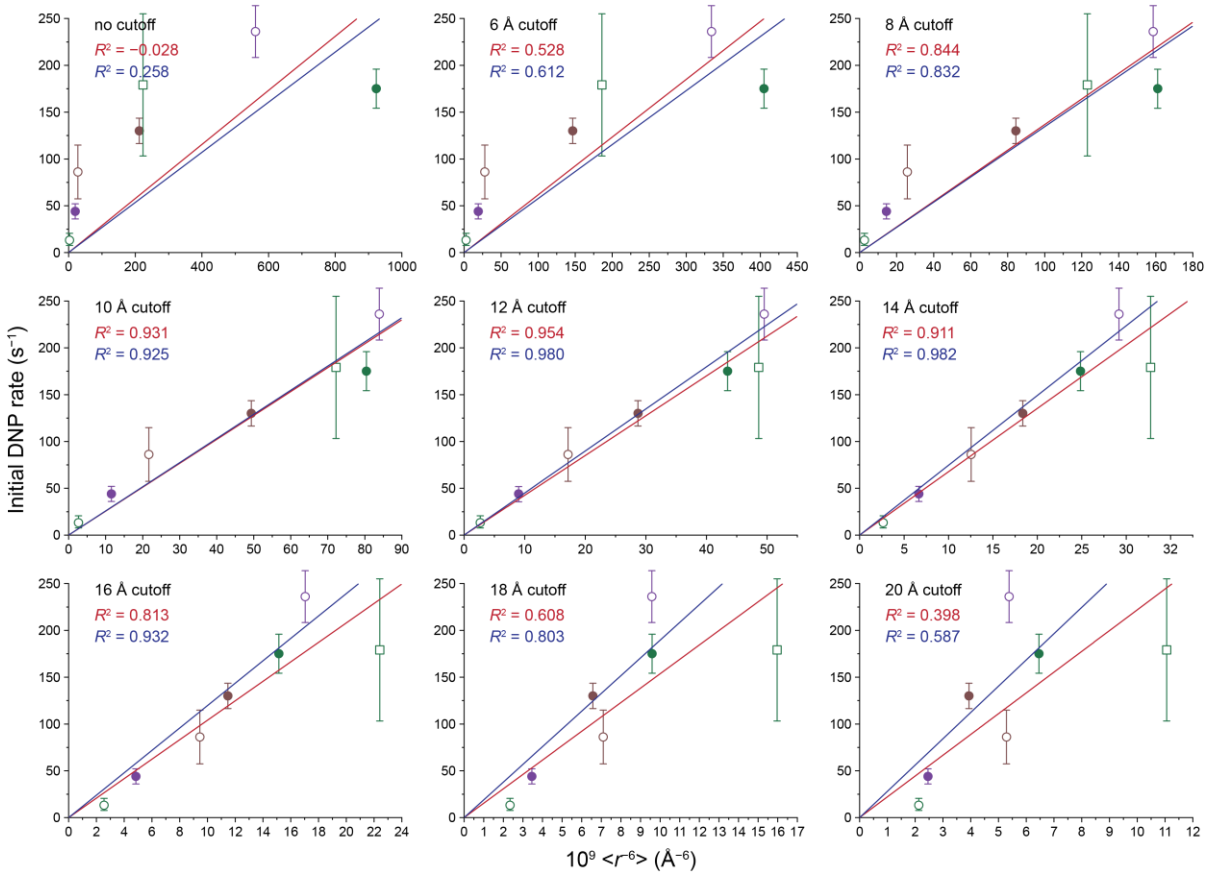

Figure S8. Plot of the experimentally measured initial DNP rate versus the effective direct ^{15}N DNP transfer rate calculated from distributed spin pairs within computational structure models with different lower distance cutoffs as is shown in Figure S5 and described in the text. Distances to Lys are shown as full circles, distances to Arg as open circles; data points from the F4C mutant are shown in green, from A28C in brown, and from G75C in purple. A linear regression fit through the origin is shown in red with the respective coefficient of determination (R^2) the blue line and R^2 value show a fit excluding the F4C His for demonstration of robustness.

References

S1. A. S. Lilly Thankamony, J. J. Wittmann, M. Kaushik and B. Corzilius, *Prog. Nucl. Magn. Reson. Spectrosc.*, 2017, **102-103**, 120-195.
S2. B. Corzilius, A. A. Smith and R. G. Griffin, *J. Chem. Phys.*, 2012, **137**, 054201.
S3. A. V. Astashkin and A. Schweiger, *Chem. Phys. Lett.*, 1990, **174**, 595-602.
S4. I. Bertini, C. Luchinat and G. Parigi, *Concepts Magn. Reson.*, 2002, **14**, 259-286.
S5. I. Solomon, *Phys. Rev.*, 1955, **99**, 559-565.
S6. D. S. Wishart, C. G. Bigam, J. Yao, F. Abildgaard, H. J. Dyson, E. Oldfield, J. L. Markley and B. D. Sykes, *J. Biomol. NMR*, 1995, **6**, 135-140.
S7. T. D. Goddard and D. G. Kneller, *Journal*.
S8. A. C. Wang, S. Grzesiek, R. Tschudin, P. J. Lodi and A. Bax, *J. Biomol. NMR*, 1995, **5**, 376-382.
S9. J. Iwahara, C. Tang and G. Marius Clore, *J. Magn. Reson.*, 2007, **184**, 185-195.
S10. J. L. Battiste and G. Wagner, *Biochemistry*, 2000, **39**, 5355-5365.
S11. M. Sjodt and R. T. Clubb, *Bio-protocol*, 2017, **7**, e2207.
S12. M. D. Hanwell, D. E. Curtis, D. C. Lonie, T. Vandermeersch, E. Zurek and G. R. Hutchison, *Journal of Cheminformatics*, 2012, **4**, 17.
S13. K. Kumar, C. A. Chang, L. C. Francesconi, D. D. Dischino, M. F. Malley, J. Z. Gougoutas and M. F. Tweedle, *Inorg. Chem.*, 1994, **33**, 3567-3575.
S14. M. Dolg, H. Stoll, A. Savin and H. Preuss, *Theor. Chim. Acta*, 1989, **75**, 173-194.
S15. C. Adamo and V. Barone, *J. Chem. Phys.*, 2002, **116**, 5933-5940.
S16. J. Tomasi, B. Mennucci and R. Cammi, *Chem. Rev.*, 2005, **105**, 2999-3093.
S17. S. Kothiwale, J. L. Mendenhall and J. Meiler, *Journal of Cheminformatics*, 2015, **7**, 47.
S18. S. Gražulis, D. Chateigner, R. T. Downs, A. F. T. Yokochi, M. Quirós, L. Lutterotti, E. Manakova, J. Butkus, P. Moeck and A. Le Bail, *J. Appl. Crystallogr.*, 2009, **42**, 726-729.
S19. S. Gražulis, A. Daškevič, A. Merkys, D. Chateigner, L. Lutterotti, M. Quirós, N. R. Serebryanaya, P. Moeck, R. T. Downs and A. Le Bail, *Nucleic Acids Res.*, 2011, **40**, D420-D427.
S20. J. K. Leman, B. D. Weitzner, S. M. Lewis, J. Adolf-Bryfogle, N. Alam, R. F. Alford, M. Aprahamian, D. Baker, K. A. Barlow, P. Barth, B. Basanta, B. J. Bender, K. Blacklock, J. Bonet, S. E. Boyken, P. Bradley, C. Bystroff, P. Conway, S. Cooper, B. E. Correia, B. Coventry, R. Das, R. M. De Jong, F. DiMaio, L. Dsilva, R. Dunbrack, A. S. Ford, B. Frenz, D. Y. Fu, C. Geniesse, L. Goldschmidt, R. Gowthaman, J. J. Gray, D. Gront, S. Guffy, S. Horowitz, P.-S. Huang, T. Huber, T. M. Jacobs, J. R. Jeliazkov, D. K. Johnson, K. Kappel, J. Karanicolas, H. Khakzad, K. R. Khar, S. D. Khare, F. Khatib, A. Khramushin, I. C. King, R. Kleffner, B. Koepnick, T. Kortemme, G. Kuenze, B. Kuhlman, D. Kuroda, J. W. Labonte, J. K. Lai, G. Lapidoth, A. Leaver-Fay, S. Lindert, T. Linsky, N. London, J. H. Lubin, S. Lyskov, J. Maguire, L. Malmström, E. Marcos, O. Marcu, N. A. Marze, J. Meiler, R. Moretti, V. K. Mulligan, S. Nerli, C. Norn, S. Ó'Conchúir, N. Ollikainen, S. Ovchinnikov, M. S. Pacella, X. Pan, H. Park, R. E. Pavlovicz, M. Pethe, B. G. Pierce, K. B. Pilla, B. Raveh, P. D. Renfrew, S. S. R. Burman, A. Rubenstein, M. F. Sauer, A. Scheck, W. Schief, O. Schueler-Furman, Y. Sedan, A. M. Sevy, N. G. Sgourakis, L. Shi, J. B. Siegel, D.-A. Silva, S. Smith, Y. Song, A. Stein, M. Szegedy, F. D. Teets, S. B. Thyme, R.

Y.-R. Wang, A. Watkins, L. Zimmerman and R. Bonneau, *Nat. Methods*, 2020, **17**, 665-680.
S21. P. D. Renfrew, E. J. Choi, R. Bonneau and B. Kuhlman, *PLoS One*, 2012, **7**, e32637.
S22. R. F. Alford, A. Leaver-Fay, J. R. Jeliazkov, M. J. O'Meara, F. P. DiMaio, H. Park, M. V. Shapovalov, P. D. Renfrew, V. K. Mulligan, K. Kappel, J. W. Labonte, M. S. Pacella, R. Bonneau, P. Bradley, R. L. Dunbrack, Jr., R. Das, D. Baker, B. Kuhlman, T. Kortemme and J. J. Gray, *J. Chem. Theory Comput.*, 2017, **13**, 3031-3048.
S23. G. Cornilescu, J. L. Marquardt, M. Ottiger and A. Bax, *J. Am. Chem. Soc.*, 1998, **120**, 6836-6837.
S24. P. Conway, M. D. Tyka, F. DiMaio, D. E. Konerding and D. Baker, *Protein Sci.*, 2014, **23**, 47-55.
S25. J. Iwahara, C. D. Schwieters and G. M. Clore, *J. Am. Chem. Soc.*, 2004, **126**, 5879-5896.
S26. V. Aladin and B. Corzilius, *Solid State Nucl. Magn. Reson.*, 2019, **99**, 27-35.